

# Journal of Biomedical Optics

[SPIEDigitalLibrary.org/jbo](http://SPIEDigitalLibrary.org/jbo)

## **Scanning-fiber-based imaging method for tissue engineering**

Matthias C. Hofmann  
Bryce M. Whited  
Josh Mitchell  
William C. Vogt  
Tracy Criswell  
Christopher Rylander  
Marissa Nichole Rylander  
Shay Soker  
Ge Wang  
Yong Xu

# Scanning-fiber-based imaging method for tissue engineering

Matthias C. Hofmann,<sup>a</sup> Bryce M. Whited,<sup>b</sup> Josh Mitchell,<sup>a</sup> William C. Vogt,<sup>b</sup> Tracy Criswell,<sup>d</sup> Christopher Rylander,<sup>b,c</sup> Marissa Nichole Rylander,<sup>b,c</sup> Shay Soker,<sup>d</sup> Ge Wang,<sup>b</sup> and Yong Xu<sup>a</sup>

<sup>a</sup>Virginia Tech, Bradley Department of Electrical and Computer Engineering, Blacksburg, Virginia 24061

<sup>b</sup>Virginia Tech, School of Biomedical Engineering and Sciences, Blacksburg, Virginia 24061

<sup>c</sup>Virginia Tech, Department of Mechanical Engineering, Blacksburg, Virginia 24061

<sup>d</sup>Wake Forest University School of Medicine, Wake Forest Institute for Regenerative Medicine, Medical Center Boulevard, Winston-Salem, North Carolina 27157

**Abstract** A scanning-fiber-based method developed for imaging bioengineered tissue constructs such as synthetic carotid arteries is reported. Our approach is based on directly embedding one or more hollow-core silica fibers within the tissue scaffold to function as micro-imaging channels (MIC). The imaging process is carried out by translating and rotating an angle-polished fiber micro-mirror within the MIC to scan excitation light across the tissue scaffold. The locally emitted fluorescent signals are captured using an electron multiplying CCD camera and then mapped into fluorophore distributions according to fiber micro-mirror positions. Using an optical phantom composed of fluorescent microspheres, tissue scaffolds, and porcine skin, we demonstrated single-cell-level imaging resolution (20 to 30  $\mu\text{m}$ ) at an imaging depth that exceeds the photon transport mean free path by one order of magnitude. This result suggests that the imaging depth is no longer constrained by photon scattering, but rather by the requirement that the fluorophore signal overcomes the background “noise” generated by processes such as scaffold autofluorescence. Finally, we demonstrated the compatibility of our imaging method with tissue engineering by visualizing endothelial cells labeled with green fluorescent protein through a  $\sim 500 \mu\text{m}$  thick and highly scattering electrospun scaffold. © 2012 Society of Photo-Optical Instrumentation Engineers (SPIE). [DOI: 10.1117/1.JBO.17.6.066010]

Keywords: molecular imaging; fiber optics; deep tissue imaging; tissue engineering; fluorescence imaging; endothelial cells; blood vessel; image processing.

Paper 12006 received Jan. 4, 2012; revised manuscript received Apr. 15, 2012; accepted for publication Apr. 17, 2012; published online Jun. 4, 2012.

## 1 Introduction

The field of tissue engineering has emerged as an important area of biomedical research, where its goal is to create functional tissues and organs in the laboratory in order to replace or restore those damaged by disease and trauma.<sup>1-4</sup> Typically, studies in tissue engineering are carried out in separate steps that involve fabricating a biocompatible scaffold capable of supporting cell growth (i.e., an artificial extracellular matrix), seeding living cells onto the scaffold, culturing the cell-seeded scaffold in a bioreactor, and then surgically implanting the preconditioned construct into a living animal to replace the damaged tissue or organ.<sup>5-7</sup>

Successful maturation of bioengineered tissues is a highly complex and dynamic process that involves extensive interactions among multiple cell types and their surrounding extracellular environment. Given its biological complexity, the process of tissue regeneration must be frequently monitored and evaluated in order to optimize tissue construct design and to improve the clinical outcome.<sup>8</sup> However, it is very difficult to achieve single-cell-level-resolution imaging at a depth beyond one photon transport mean free path (TMFP).<sup>9,10</sup> As a result, the current “gold standard” for evaluating tissue constructs remains histological analysis, which requires sacrificing separate specimens at different time points by dissecting them into thin slices and

then examining the slices under an optical microscope. These destructive methods are time consuming, labor intensive, and cannot reveal cell behaviors and interactions in their natural microenvironments. Consequently, the inability to perform deep-tissue imaging at single cell resolution has become a major barrier in tissue engineering research.

Accomplishing high-resolution deep-tissue imaging is a difficult challenge that goes far beyond tissue engineering. In fact, a major problem in biophotonics is the conflict between imaging depth and imaging resolution. Fundamentally, the difficulty in simultaneously achieving a high imaging resolution and a large imaging depth can be traced to this observation: Most biological tissues are turbid media and therefore strongly scatter light. Even for recently developed modalities such as photoacoustic imaging, the spatial resolution is approximately  $>50 \mu\text{m}$  at the imaging depth of three photon TMFP.<sup>11,12</sup> On the other extreme, there are various tomographical techniques such as fluorescence molecular tomography, where one can achieve a large imaging depth ( $\sim 2 \text{ mm}$ ) by sacrificing imaging resolution to the level of  $>500 \mu\text{m}$ .<sup>9</sup>

The inability to non-destructively monitor tissue development, which often requires deep-tissue, single-cell-level resolution imaging, poses a significant hindrance for tissue engineering research. A specific example is the bioengineering of synthetic vascular grafts.<sup>13,14</sup> In this case, successful clinical outcome depends critically on the coordinated endothelial cell

Address all correspondence to: Yong Xu, 467 Whittemore Hall, Virginia Tech, Blacksburg, Virginia 24060. Tel: +540 231 2464; Fax: +540 231 3362; E-mail: [yong@vt.edu](mailto:yong@vt.edu)

(EC) coverage on the lumen (inner surface) of the blood vessel graft.<sup>15</sup> However, since the thickness of the blood vessel scaffold must significantly exceed one photon TMFP in order to withstand normal blood pressure, it is difficult to apply existing imaging methods to “see” through the optically opaque scaffold and monitor EC behaviors on the scaffold lumen.

This manuscript reports a novel imaging method that can overcome the aforementioned challenge. Our approach is based on embedding flexible micro-imaging channels (MICs) directly into a vascular scaffold. Each MIC serves as a guiding channel through which we can insert a fiber micro-mirror and locally scan excitation light across a region of interest (ROI) on the scaffold lumen. After collecting fluorescent signals generated during fiber scanning, we can map the values of these signals onto a digital grid and reconstruct the spatial distributions of the fluorescently labeled ECs. A major advantage of our method is that the link between imaging resolution and imaging depth is “decoupled,” making it possible to greatly increase imaging depth without significantly sacrificing imaging resolution. Using a tissue scaffold phantom, we demonstrated that our imaging system could deliver 20 to 30  $\mu\text{m}$  imaging resolution at an imaging depth of approximately three photon TMFPs. Furthermore, the resolution of our imaging system remained essentially the same even if the total imaging depth was increased by an additional eight photon TMFPs. Given the results of this phantom study, our imaging method has the potential to find a wide range of tissue engineering applications that involve epithelial tissues.

## 2 Materials and Methods

### 2.1 Phantom Design and Fabrication

#### 2.1.1 Experimental design

In Fig. 1(a), we show a pulsatile flow bioreactor developed for the preconditioning of a synthesized vascular graft.<sup>16</sup> As shown in the figure, the vascular graft is enclosed in a sealed bioreactor and cannot be easily imaged using traditional optical imaging methods. Ultimately, we intend to use the scanning-fiber-based imaging method to assess lumen endothelialization, where a MIC is directly embedded into the scaffold wall as shown in Fig. 1(b). However, before applying this novel imaging method for any *in vitro* or *in vivo* studies, we need to first validate system performance through optical phantom studies.

As illustrated in Fig. 1(c), fluorescent labeled ECs exist only on the innermost layer (i.e., lumen) of the tubular scaffold. Consequently, it is difficult to apply direct-line-of-sight optical microscopy to visualize luminal fluorophore distributions through the optically opaque scaffold. Yet in order to validate our imaging method, we need to compare the results obtained through fiber scanning with a common standard such as direct-line-of-sight microscopy. To resolve this quandary, we created an equivalent phantom by “flattening” the tubular vessel and converting it to a planar structure, as illustrated in Fig. 1(d). Because ECs cover only the innermost surface of a blood vessel, they will exist only on one side of the “flat” vessel surface, which is referred to as the “luminal” surface. Note that the objective lens and all other instruments required for scanning-fiber-based imaging should be placed outside of the animal body as indicated by the “detector” in Fig. 1(c) and 1(d). Hence we denote the surface opposite of the luminal surface as the “exterior” surface. With these considerations, the

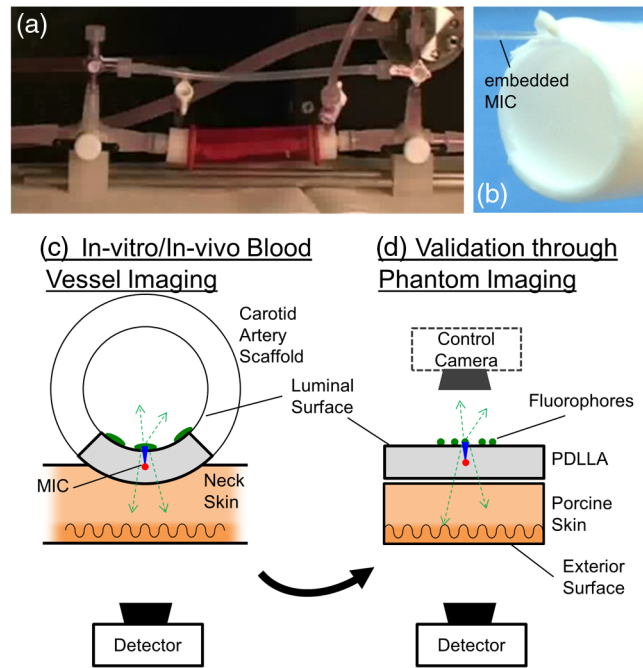


**Fig. 1** (a) A pulsatile flow bioreactor for *in vitro* incubation of bioengineered carotid artery scaffolds developed by one of the authors. Bioreactors often require a hermetically enclosed chamber that is incompatible with standard optical imaging methods. (b) A vascular scaffold embedded with a micro-imaging channel (MIC) for non-destructive, scanning-fiber-based imaging. (c) and (d) Depict design of a planar optical phantom that imitates a tubular carotid artery scaffold graft for future *in vitro* (no neck skin) or *in vivo* (with neck skin) studies. As shown in (c), an MIC is directly embedded within the wall of the scaffold. Through the MIC, we can deliver highly localized excitation light to a region of interest on scaffold lumen and generate a fluorescent signal. Part of the fluorescent signal is captured by an external detector for image reconstruction. (d) An optical phantom model was designed to mimic the experimental configuration in (c). The phantom is designed such that we can verify our fluorescence mapping results using the direct-line-of-sight images obtained by a control camera.

optical phantom used in this study is composed of a planar tissue scaffold with an embedded MIC, a piece of porcine skin, and multiple fluorophores placed on the luminal surface. With the configuration depicted in Fig. 1(d), we can easily obtain the direct-line-of-sight images as control images that accurately depict the distributions of fluorophores on scaffold lumen. Physical properties of the phantom such as scaffold porosity and optical coefficients were kept equivalent to the vessel scaffolds used for carotid artery engineering.<sup>17</sup>

The presence of the 3-mm thick porcine skin serves two purposes. First, it mimics *in vivo* conditions,<sup>18</sup> where the presence of additional obstructive biological tissues, such as the skin of an animal, must be included in order to account for additional photon scattering and autofluorescence. Additionally, the porcine skin also enables us to evaluate the performance of our imaging system as we significantly increase imaging depth.

We used two types of fluorophores in our studies. To evaluate the resolution and depth dependence of the imaging system, we used 28- $\mu\text{m}$ -diameter green fluorescent microspheres (FP-30052-5, Spherotech Inc., Lake Forest, IL) to simulate green fluorescent protein (GFP)-labeled ECs. For a preliminary live cell study, we used GFP-labeled ECs seeded on the luminal surface of a flat 500  $\mu\text{m}$  thick scaffold.

### 2.1.2 Scaffold fabrication

Electrospinning was used to fabricate a scaffold to construct the phantom.<sup>19</sup> Briefly, bioabsorbable poly-(D, L-lactide) (PDLLA) ( $M_w = 80,000$  g/mol, SurModics Pharmaceuticals, Birmingham, AL) was suspended in a 22% w/v solution with a 3:1 ratio of tetrahydrofuran:dimethylformamide (Fisher Scientific, Fair Lawn, NJ) under gentle stirring for 4 h. Next, the polymer solution was delivered at a flow rate of 5 ml/hr through an 18 G blunt-tip needle attached to the end of a syringe. A 13 kV charge was then applied between the needle tip and a 2-in. diameter aluminum mandrel using a direct current power supply (Gamma High Voltage Research, Ormond Beach, FL). The mandrel was placed 10 cm away from the needle tip and set to rotate at a constant 60 rpm. The high voltage difference between the needle tip and the spinning mandrel drew the charged polymer solution towards the mandrel. The rapid evaporation of the solvent then generated thin strands of PDLLA polymer fibers ( $\sim 1$   $\mu\text{m}$  in diameter), which formed a finely woven scaffold sheet on the spinning mandrel as shown up close by the SEM image in Fig. 2(a). Once the scaffold sheet reached its desired thickness, it was removed from the mandrel and placed in a desiccator for 10 h to remove any residual solvent.

### 2.1.3 MIC integration

A sintering process was adapted<sup>20</sup> to selectively incorporate the MICs into the PDLLA scaffold. The MICs are made of a custom-sized, optically transparent and flexible, fused-silica hollow fiber (Polymicro Technologies, Phoenix, AZ) with an inner and outer diameter of 145 and 240  $\mu\text{m}$ , respectively. Our MIC integration process is as follows. First, a PDLLA sheet was electrospun to 300  $\mu\text{m}$  thickness and then cut into 3 cm  $\times$  2 cm rectangular mats. Next, we placed MICs on top of a PDLLA mat and covered it with a second mat, effectively sandwiching the MICs between the two scaffold mats. The scaffold mats were then compressed between glass slides with a 28 g weight in an oven at 54°C for 20 min followed by a 10 min cool down period. Through the heated compression, the PDLLA mats fused together without losing the original woven structure, while securely embedding the MICs inside as shown in Fig. 2(a). After sintering, the total thickness of the sample was

$500 \pm 9$   $\mu\text{m}$  and the distance from the luminal surface to the center of the MIC was  $\sim 200$   $\mu\text{m}$ .

### 2.2 Excitation Light Delivery

Delivery of pump light for fluorescence excitation was achieved by inserting an angle-polished fiber micro-mirror into the transparent MIC as shown in the image in Fig. 2(b). The mirror was fabricated by polishing the tip of a standard single mode fiber (SMF430, Nufern Inc., East Granby, CT) at a 45 deg angle with a 0.1- $\mu\text{m}$  grit diamond lapping film (Pace Technologies, Tucson, AR). Excitation light was coupled into the optical fiber and perpendicularly redirected by the 45 deg air-silica interface via total internal reflection as shown in Fig. 2(c). After inserting the micro-mirror into the MIC, the propagation direction of the excitation light was controlled through the translational and angular position of the inserted fiber micro-mirror.

### 2.3 Incorporation of Fluorescent Sources

The phantom studies required placing fluorescent sources on the scaffold lumen at fixed locations. We used 28  $\mu\text{m}$  diameter microspheres coated with a green fluorescent dye (FP-30052-5, Spherotech Inc., Lake Forest, IL) to mimic GFP-labeled ECs. First, the microspheres were suspended in deionized water at a 1:10 volume ratio. Next, we pipetted 1 ml of the solution onto the lumen of the phantom, which lead to a random dispersion of the microspheres. To securely attach the microsphere to the scaffold surface, a thin  $\sim 10$   $\mu\text{m}$  layer of additional PDLLA was electrospun on top of the microspheres. The added layer was thin enough to be optically transparent, yet sufficiently strong to eliminate any change in microsphere pattern during extended handling of the phantom.

### 2.4 Measuring the Scaffold Optical Properties

To quantify the optical characteristics of the electrospun PDLLA scaffold, a spectrophotometer (Cary 5000, Agilent Technologies, Santa Clara, CA) coupled with an integrating sphere (Labsphere, North Sutton, NH) was used to measure the reflectance and transmittance values from 450 to 750 nm. The optical measurements were repeated on three scaffold mats having the same thickness as the phantom ( $\pm 25$   $\mu\text{m}$  std.dev.). Prior

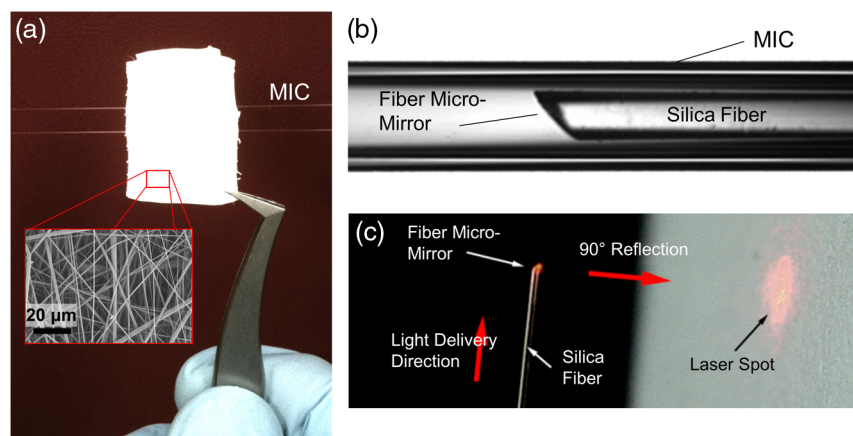


**Fig. 2** (a) A thinly woven PDLLA scaffold mat was electrospun and then cut into 3 cm  $\times$  2 cm rectangular mats. The optically turbid scaffold architecture is shown in the scanning electron microscope image. The PDLLA phantom was fabricated by placing micro-imaging channels (MICs) between two scaffold mats and heat sintering them together. (b) A microscope image of a fiber micro-mirror inserted into a MIC. (c) The 90 deg reflection of the excitation light at the polished fiber tip is used for local delivery and scanning of excitation light within the region of interest.

to the measurements, the scaffolds were immersed and saturated in Endothelial Growth Medium-2 (Lonza Biomedical, Walkersville, MD), the same cell media used for EC culturing and phantom imaging. From the reflectance and transmittance values, the absorption coefficient  $\mu_a$ , and scattering coefficient  $\mu_s$ , were calculated using the inverse adding-doubling algorithm developed by Prahl.<sup>21</sup> For the calculations, we used commonly accepted values for the refractive index ( $n = 1.38$ ) and anisotropy number ( $g = 0.9$ ) of the scaffold.<sup>9,22</sup> We calculated the MFP distance of the PDLA by using

$$\text{MFP} = \frac{1}{\mu_s}, \quad (1)$$

which models the average distance covered by a photon until a scattering event occurs. A photon undergoing several scattering events can be approximated by the TMFP based on the anisotropy number  $g$  (which relates to the degree of forward scattering) and is defined as

$$\text{TMFP} = \text{MFP} \times \frac{1}{(1 - g)}. \quad (2)$$

## 2.5 Imaging System

The scanning-fiber-based imaging method requires local excitation of the fluorophores using the fiber mirror and the detection of fluorescent signals generated at each mirror location. A schematic and a photograph of the imaging platform that can accommodate this design is shown in Fig. 3(a) and 3(b), respectively. A 473-nm laser light was coupled into an optical fiber and delivered to the sample's ROI by the fiber micro-mirror within the MIC. The laser was operated at a continuous 1 mW, with a fiber injection efficiency of  $\sim 15\%$ . The movement of the fiber micro-mirror was controlled by a custom-built two-axis

motorized scanning system consisting of a  $0.1\text{-}\mu\text{m}$ -resolution translation stage (UTM100PP.1HL, Newport, Irvine, CA) and a  $20\text{ deg/sec}$  rotation stage (URM80PE, Newport). A fiber clamp was mounted to the scanner that held the fiber in place. The distance from the fiber micro-mirror to the clamp was 15 cm. This system enabled the control of both the angular and the translational forward/backward movement of the fiber micro-mirror using a custom Labview program (National Instruments, Austin TX). The fluorescent responses generated by the fluorophores were collected by a  $2\times$  long-working distance lens (M Plan Apo 2, Mitutoyo) and captured by the electron multiplying CCD camera (EM-CCD) (iXon, Andor Inc., Belfast). The distance between the lens and the phantom was 10 cm. For fluorescence mapping, the camera was set to a full-binning mode where the EM-CCD chip's pixels were internally summed together to provide the total fluorescence intensity. In principle, we can replace the camera with a single detector such as a photomultiplier tube. However, a camera is required to quantify fluorescence distributions on the scaffold exterior surface that will be shown later. A bandpass filter (525/45 BrightLine, Semrock, Rochester, NY) was used to remove the excitation light from fluorescence signals.

## 2.6 Fiber-Scanning and Fluorescence-Mapping Procedure

The key feature of the scanning-fiber-based method is the localized fluorophore excitation. More specifically, after using the fiber mirror to deliver excitation light into the scaffold, we can assume all fluorescent signals are generated within this highly localized light spot on the luminal surface. This local light spot is referred to as an "excitation spot" and its location on the lumen is controlled by the fiber mirror position within the MIC. The illustration in Fig. 3(c) shows the excitation spot as it appears on the lumen.

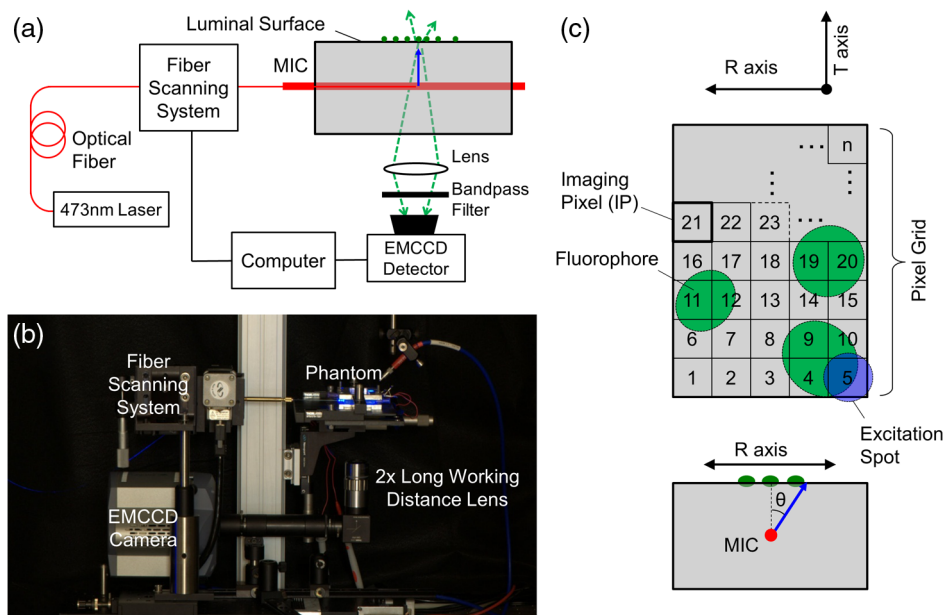


**Fig. 3** (a) Schematic and (b) photograph of the scanning-fiber-based imaging system. (c) Diagram of the imaging procedure. Using the fiber mirror, we can locally deliver excitation light to a point within the region of interest (ROI) (excitation spot). The excitation spot is moved within the ROI by rotating and translating the fiber mirror. By scanning the excitation spot according to a pixel grid, we can map the intensity responses into a digital grid to obtain fluorophore distribution.

The scanning system possesses two degrees of freedom: one is the forward/backward translation  $x$  and the other is angular rotation  $\theta$  of the fiber inside the MIC. As the excitation spot is scanned across the lumen, a fluorescence response is generated if the spot overlaps with a fluorophore. A portion of the fluorescent signal travels through the optically opaque phantom and is captured by the detector. Since all fluorescent signals are produced within the spatially-localized excitation spot, we can “reconstruct” the fluorophore distribution by using the intensity of the fluorescence signal captured by the detector. This reconstruction process is referred to as “fluorescence mapping”, and is described in detail below.

First, we selected a ROI on the lumen and divided it into a pixel grid of  $5 \times 5 \mu\text{m}^2$  imaging pixels (IP) as illustrated in Fig. 3(c). Every IP in the grid can be selectively illuminated by the excitation spot by establishing a one-to-one correspondence between the center of the spot (e.g.,  $R$  axis and  $T$  axis) and the corresponding fiber mirror position ( $x, \theta$ ). In Fig. 3(c), we define the  $R$  axis as parallel to the MIC and the  $T$  axis as perpendicular to the MIC. Note that the coordinate  $R$  is a function of the fiber rotation angle  $\theta$  and  $T$  is directly given by the linear translation  $x$  of the fiber mirror. Furthermore,  $\theta = 0$  denotes the case where the excitation light is launched directly towards the lumen.

To begin an experiment, the excitation spot was first positioned to IP = 1. The resulting fluorescence signal response value was collected by the detector and assigned to IP = 1. This process was repeated for each IP in the pixel grid by discretely scanning the excitation spot across the luminal surface. By plotting the response intensities of each IP in the pixel grid as a 2-D intensity array, we obtained a mapped image of the fluorophore distribution on the luminal surface.

To intuitively understand the validity of this imaging method, let us consider an ideal case that satisfies the following assumptions: (1) the excitation spot is contained entirely within any given IP, (2) the excitation light intensity remains constant across the lumen surface for all fiber mirror locations, and (3) the scaffold does not generate any background fluorescence (i.e., autofluorescence) as “noise.” In this ideal case, the fluorescent response assigned to each IP should be directly proportional to the brightness of the fluorophores within the corresponding IP. As a result, the image obtained through fluorescence mapping should accurately reflect the spatial distributions of fluorophores over the lumen.

This intuitive analysis also identifies three factors that may limit the performance of the fluorescence mapping method including: (1) the excitation spot may exceed the size of an IP; (2) the excitation light intensity may not remain constant over the luminal surface; and (3) the scaffold may generate autofluorescence that overwhelms the fluorescent signals produced by the fluorophores. The impacts of these three factors will be discussed in Sec. 3.

### 2.7 Excitation Spot Characterization

The intensity profile of the excitation spot was characterized using a control camera (XCD-X710, Sony, Japan) as depicted in Fig. 2(b). The camera lens was focused on the luminal surface of the phantom and pictures were taken of the excitation spot. After inserting the fiber mirror into the MIC, the excitation light was launched towards the lumen, producing a different spot profile at a given launching angle  $\theta$ , and then captured by the camera as an image. The results are described in Sec. 3.1.

### 2.8 Spectrum Measurement

The spectra of fluorescent signals as well as “noises” generated by scaffold or porcine skin autofluorescence were measured by replacing the EM-CCD camera with a spectrometer (USB2000, OceanOptics, Dunedin, FL). The imaging system remains the same otherwise.

### 2.9 Cell Culture Protocol

A human microvascular endothelium cell line (American Type Culture Collection (ATCC), Manassas, VA) labeled with enhanced GFP was used to demonstrate that our imaging method is suitable for *in vitro* and *in vivo* tissue engineering. All cells were cultured in Endothelial Growth Medium-2 (EGM-2) (Lonza Biomedical, Walkersville, MD). Before cell seeding, the scaffold with embedded MICs was sterilized using 70% ethanol for 30 min, followed by three sterile phosphate buffered saline (PBS) washes for 10 min each. The ECs were then suspended in 100  $\mu\text{L}$  of media and seeded onto the scaffold at a density of  $1 \times 10^4$  cells/cm<sup>2</sup>. The scaffold was then placed in the incubator for two hours to allow cell attachment and then was gently washed with PBS to remove any unattached cells.

## 3 Results

### 3.1 Excitation Spot Characterization

The spatial resolution of our imaging method is largely determined by the size of the excitation spot on the lumen. Therefore, it is important to quantify the properties of the excitation spot as a function of the fiber mirror launching angle  $\theta$ . The configuration described in Sec. 2.8 was used to obtain the results shown in Fig. 4(a)–4(c). The angle  $\theta$ , defined in Fig. 3(c), was swept from  $\theta$  equals to  $-50$  deg to  $+50$  deg in 1 deg increments on five different locations on the  $T$  axis. The characteristic data of the excitation spot presented in Fig. 4 shows both the average as well as the standard deviation of the five distinct  $T$  axis locations.

Figure 4(a) shows the full-width-half-maximum (FWHM) of the excitation spot size as a function of the launching angle  $\theta$ . Several intensity profiles of the excitation spot on the luminal surface are also shown in the figure as insets. It is clear that the FWHM increased as the launching angle deviated from  $\theta = 0$  deg. This phenomenon can be explained by the fact that at the angle of  $\theta = 0$  deg, excitation photons encountered the least number of scattering events as they traveled through the scaffold to the lumen. As the angle  $|\theta|$  increased, excitation photons traveled a longer distance to the lumen, thereby experiencing more scattering within the scaffold. As a result, the FWHM of the excitation spot increased as a function of the launching angle  $\theta$ . For the results in Fig. 4(a), the excitation spot FWHM was at  $21 \pm 0.8 \mu\text{m}$  at  $\theta = 0$  deg and increased by roughly 2.5 times to  $50 \pm 8.2 \mu\text{m}$  at  $\theta = \pm 50$  deg.

In Fig. 4(b), we show that the total intensity of the excitation spot decreased as  $|\theta|$  increased. The intensity value was calculated by summing all CCD camera pixel counts within the excitation spot [i.e., inset in Fig. 4(a)]. A possible explanation for this behavior is that at a larger launching angle  $|\theta|$ , the excitation photons traveled a longer distance, therefore experiencing more absorption before reaching scaffold lumen. Since the fluorescence response has a linear dependence on excitation light intensity, the fluorescence signals captured during fluorescence

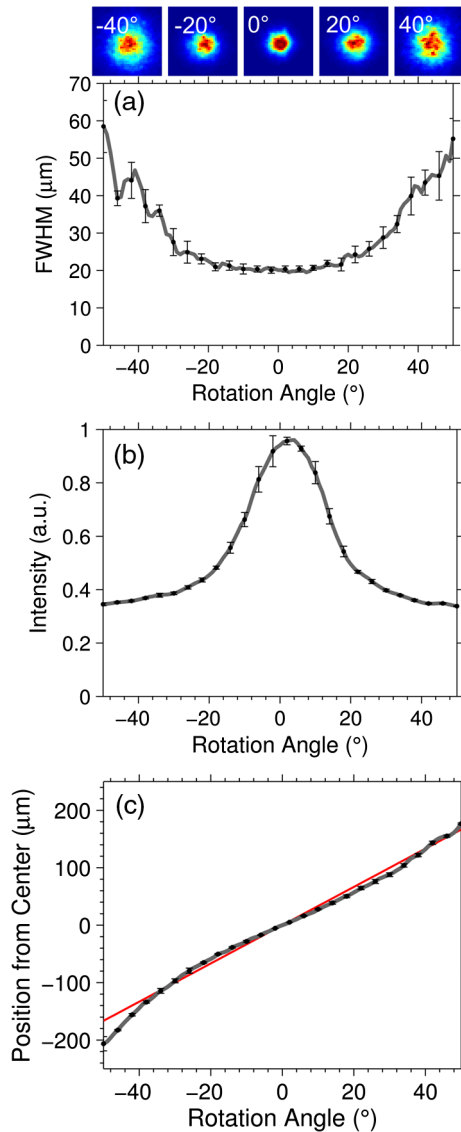


**Fig. 4** Excitation spot characterization. The plot lines are in 1 deg increments and the error is shown at every 4th point to prevent overcrowding. Error bars represent one std. dev. centered at the mean of the five trials. (a) The full-width-half-maximum of the excitation spot intensity profile on scaffold lumen is shown with respect to launching angle  $\theta$ . The insets depict the actual excitation spot profile with  $|\theta|$  equal to 0, 20, and 40 deg, respectively. (b) The intensity of the profile (summed pixels) shows a diminishing excitation spot strength at increasing angles  $|\theta|$ . (c) The excitation spot profile center position on the  $R$  axis is shown to behave nearly linearly with respect to  $|\theta|$ . From the results, we find that  $R(\theta) = 3.33 \times \theta$  based on a linear fit (red).

mapping must be renormalized as follows: At each  $|\theta|$  value, the magnitude of the fluorescent signal was boosted according to the curve in Fig. 4(b) so that the “renormalized” excitation intensity remains constant for all pixels.

Figure 4(c) shows that along the  $R$  axis, the center position of the excitation spot depends almost linearly on the fiber mirror launching angle  $\theta$ . Using a linear fit, we can relate the position of the excitation spot along the  $R$  axis versus the launching angle as  $R(\theta) = 3.33 \times \theta$ . This result indicates that for this phantom, the excitation spot can scan across a distance of 400  $\mu\text{m}$  (200  $\mu\text{m}$  on either side of  $\theta = 0$ ) on the lumen along the  $R$  axis, with a FWHM ranging from 21 to 50  $\mu\text{m}$ . The scanning range along the  $T$  axis is unlimited.

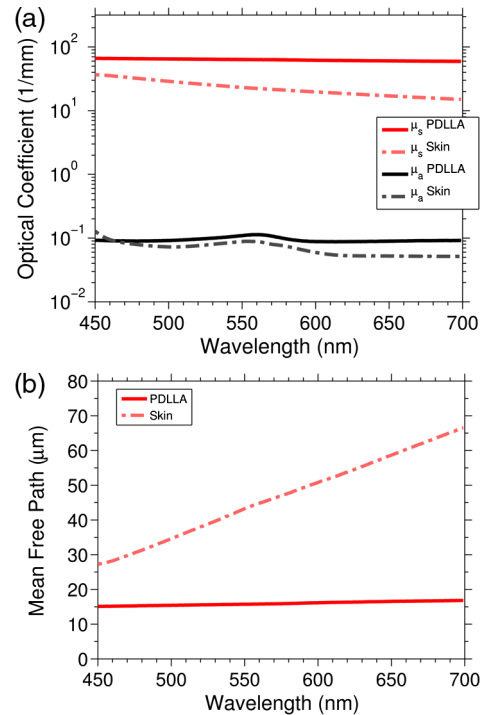


**Fig. 5** (a) The scattering coefficient ( $\mu_s$ ) of PDLLA is found to be roughly double that of porcine skin over the 450 to 700 nm range. The results also show that scattering events ( $\mu_s$ ) dominate over absorption events ( $\mu_a$ ) by more than two orders of magnitude. (b) The mean free path for PDLLA and for porcine skin.

### 3.2 Phantom Optical Properties

The optical properties of electrospun PDLLA and porcine skin (dermis and epidermis) were measured between 450 to 700 nm to determine their absorption and scattering coefficients  $\mu_a$  and  $\mu_s$ , respectively. Such values quantitatively indicate how strongly the medium absorbs and scatters light. In Fig. 5(a) we see that optical scattering is significantly stronger than optical absorption by more than two orders of magnitude. This result suggests that the resolution of optical imaging is primarily limited by optical scattering in highly turbid biological media.

Using Eq. (1) from Sec. 2.5, we can calculate the MFP of both the PDLLA and the porcine skin. The same anisotropy factor ( $g = 0.9$ ) for the  $\mu_a$  and  $\mu_s$  calculation was used to calculate the MFP, which translates to  $\text{TMFP} = 10 \times \text{MFP}$ .<sup>21</sup> Figure 5(b) shows that at the peak fluorophore emission wavelength (510 to 530 nm), the MFP is roughly 16  $\mu\text{m}$  for PDLLA and 37  $\mu\text{m}$  for porcine skin. Based on these values, the TMFP is 160  $\mu\text{m}$  for PDLLA and 370  $\mu\text{m}$  for porcine skin. We note that even for advanced modalities such as confocal and two-photon microscopes, the imaging depth is roughly limited to 1 to 2 photon TMFP,<sup>9,23,24</sup> which, in the case of our PDLLA scaffold and porcine skin phantom, is significantly less than their corresponding thickness:  $\sim 0.5$  mm for PDLLA scaffold and  $\sim 3$  mm for porcine skin.

### 3.3 Phantom Imaging Results

In testing the accuracy of our imaging method, we first captured a control image of the fluorescent microsphere distribution on the phantom lumen surface. As described in Sec. 2.1, the control image was obtained using a standard optical microscope setup to

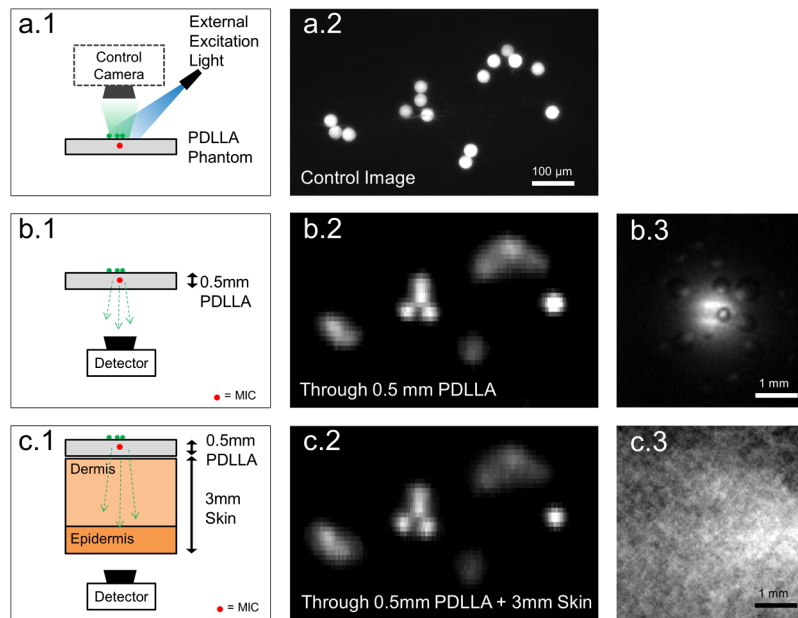


**Fig. 6** Results of fluorescence mapping. (a.1) A schematic showing how we obtain a direct-line-of-sight control image of the scaffold lumen. (a.2) An example of a control image. (b.1) Configuration for fluorescence mapping through the 0.5 mm thick PDLLA scaffold. (b.2) Mapping result through 0.5 mm PDLLA. (b.3) The spatial distribution of fluorescence signals on the bottom surface of the phantom, as captured by the EM-CCD camera. The fluorescent signals were generated by the same region of interest in (b.2) under illumination by the external excitation light. (c.1) Configuration for fluorescence mapping through the same 0.5 mm thick PDLLA scaffold and a piece of 3 mm thick porcine skin. (c.2) Results of fluorescence mapping through 0.5 mm PDLLA + 3 mm skin. (c.3) Fluorescence image on the bottom surface of the porcine skin as captured by the EM-CCD camera. We notice further “blurring” of the fluorescent signal in (c.3), yet the result of fluorescence mapping in (c.2) remain the same as the result in (b.2), which was obtained using only PDLLA scaffold.

provide an unobstructed, direct-line-of-sight, view of the luminal surface as illustrated in Fig. 6(a.1).

Prior to imaging, the sample was soaked with EGM-2. Next, the phantom was securely fastened on a glass slide. The slide with the phantom was then placed on the imaging platform and the fiber mirror was inserted into the MIC. Fiber scanning was carried out in the ROI that coincides with the control image shown in Fig. 6(a.2). After following the mapping procedure described in Sec. 2.7, we obtained the mapped image shown in Fig. 6(b.2). This configuration mimicked an *in vitro* environment of a bioengineered blood vessel with visual access to the outside surface of the vessel. When comparing the control image with the mapped image, we observe that the center position of each microsphere is in good agreement. Since the FWHM of the excitation spot is at times larger than the microsphere diameter, individual microspheres are blurred together.

Next, a 3-mm thick piece of porcine skin with an intact dermis and epidermis layer was placed under the phantom, thus further obstructing the lumen from the detector. This configuration is shown in the diagram of Fig. 6(c.1), which mimics an *in vivo* environment for a carotid artery imaging experiment. After the scanning algorithm was performed in the identical ROI, the fluorescence mapped image in Fig. 6(c.2) was produced. When comparing the fluorescence mapped image using the 0.5 mm PDLLA configuration versus the 0.5 mm PDLLA + 3 mm skin configuration, we observe that there is no significant degradation in image resolution. Therefore, the results in Fig. 6 directly demonstrate that the scanning-fiber-based method can decouple the link between imaging depth and image resolution. Fundamentally, this decoupling is due to the fact that our imaging system is not limited by the thickness of the turbid media between the lumen and the detector, but rather depends

on the signal-to-noise (SNR) of fluorescent signals. For a detailed analysis of SNR, refer to Sec. 3.5.

To compare how a standard fluorescence microscope performs in terms of resolution, we use the EM-CCD camera to capture fluorescence images on the bottom surface of the phantom, where the entire ROI on scaffold lumen was illuminated using an external excitation source. The images in Fig. 6(b.3) and Fig. 6(c.3) show the fluorescence response after traveling through 0.5 mm PDLLA and 0.5 mm PDLLA + 3 mm skin, respectively. Both images show that it is impossible to deduce the original microsphere distribution, and that adding additional turbid medium (porcine skin) causes a significant spread in the spatial distributions of fluorescent signals.

### 3.4 Imaging Resolution Analysis

We note that the result of fluorescence mapping can be modeled as a convolution of the control image with a point spread function (PSF), where the PSF describes the image “blurring” due to the finite size of the excitation spot. Mathematically, the spatial dimension of the PSF should correspond to the overall image resolution of our system.

Therefore, to quantify the overall image resolution of the fluorescence mapped image in Fig. 6, we carried out the following mathematical analysis. First, we convolved the control image with a variable-size Gaussian PSF. We note that the excitation spot profile can be closely approximated by a Gaussian PSF. By sweeping the FWHM of the Gaussian PSF from 0 to 50  $\mu\text{m}$ , we obtained various theoretically predicted fluorescence mapped images with an image resolution varying from 0 to 50  $\mu\text{m}$ . Then, the mean square error (MSE) was calculated between the theoretically predicted fluorescence mapped images

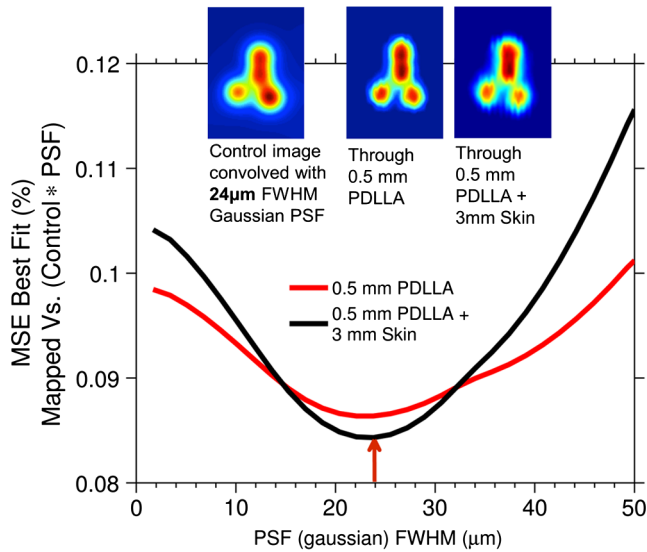


**Fig. 7** The resolution of the scanning-fiber-based method is modeled by convolving the control image with a variable Gaussian point spread function creating a theoretical mapped image. By finding the least mean square error of the difference between the theoretical and experimental results, we find the approximate resolution of the system. The result suggests that the imaging resolution is between 20 to 30  $\mu\text{m}$  at an imaging depth corresponding to 0.5 mm PDLLA plus 3 mm porcine skin.

versus the actual mapped images [i.e., the results shown in Fig. 6(b.2) or Fig. 6(c.2)]. The percentage of MSE versus the FWHM of the Gaussian PSF is plotted in Fig. 7, which shows that the smallest MSE occurs at around a 24  $\mu\text{m}$  FWHM for both with or without additional porcine skin. This matches very well with the experimental results shown at in Fig. 4(a) from  $|\theta| \sim 0$  to 30  $\mu\text{m}$ . The inserts in Fig. 7 show the experimental mapped images (through 0.5 mm PDLLA or 0.5 mm PDLLA + 3 mm skin) as well as the theoretically predicted image using a 24  $\mu\text{m}$  FWHM Gaussian PSF. With the result in Fig. 7, we conclude that the resolution of our imaging system can reach the level of 20 to 30  $\mu\text{m}$  with an imaging depth corresponding to 0.5 mm PDLLA scaffold plus 3 mm porcine skin.

### 3.5 Signal Versus Noise

Figure 8 shows the spectral components of the fluorescent signals and noises generated by the microspheres and the two phantoms, respectively. These results were obtained by replacing the EM-CCD camera with a spectrometer. Specifically, the microsphere signal was measured by positioning the excitation spot to the center of a single standing microsphere and capturing the fluorescence emission spectrum. Then, we applied the same procedure to characterize noises generated by the optical phantoms. To ensure that only “noise” was captured by the spectrometer, we positioned the excitation spot on a luminal surface location that was void of any microspheres. (We used the control camera to ensure no fluorescent microspheres exist within the excitation spot.) The results are shown in Fig. 8, where we normalized the intensity of all emission spectra such that the peaks of the spectral noise were set to be one.

We define the SNR of the imaging system as the ratio between the microsphere signal and the background noise. For the 0.5 mm PDLLA experiment, the SNR is around 4 in the 510 to 540 nm range. After adding the 3-mm thick skin, the SNR dropped to two. Although a SNR of two is relatively small, it is sufficient to separate the signal from the noise to obtain the fluorescence mapped image in Fig. 6(c.2). However, if we place a thicker tissue between the phantom and the detector such that the SNR approaches unity, it would be very difficult to separate the microsphere signals from background “noises” generated by the scaffold as well as the surrounding tissue.

The results in Fig. 8 suggest that the main limitation on fluorescence mapping lies in making sure the intensity of fluorescence signals is greater than the background noise. In other words, the spatial profile of the fluorescent signal captured on the exterior surface of the scaffold or porcine skin plays no role in fluorescence mapping—only the total strength of the fluorescent signal does. More specifically, after adding the porcine skin, the fluorescence light was distributed within a much wider spatial region [Fig. 6(c.3)] compared to the case without any porcine skin [Fig. 6(b.3)]. Yet the images obtained through fluorescence mapping did not show any significant difference. Consider the following two observations: (1) for most biological tissues, optical scattering significantly exceeds optical absorption as shown in Fig. 5, and (2) the

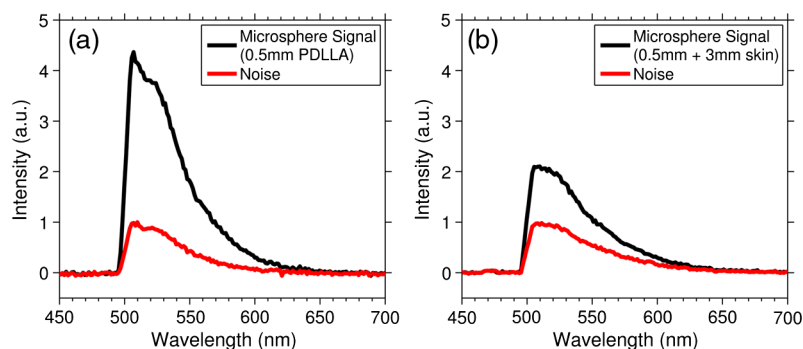


**Fig. 8** Spectral responses of microsphere signals as well as autofluorescence noises. The microsphere signal was obtained by centering the excitation spot on a single microsphere placed on the phantom lumen. The autofluorescence noise was obtained by moving the excitation spot to a location on the lumen that was free of microspheres. The signal-to-noise (SNR) is calculated as the microsphere signal divided by the autofluorescence. (a) The SNR through 0.5 mm PDLLA is around four between 510 to 545 nm. (b) The SNR through 0.5 mm PDLLA + 3 mm porcine skin is around two between 510 to 545 nm.

primary impact of photon scattering is the blurring of the fluorescent signal without significantly changing its total strength. With these considerations, it is clear that the resolution is no longer limited by the scattering of the fluorescent signal. As a result, the imaging resolution of the scanning-fiber-based method is largely “decoupled” from the total imaging depth.

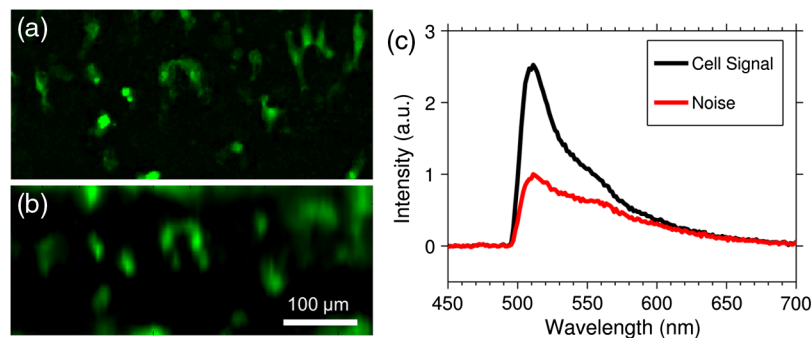
### 3.6 Endothelial Cell Imaging

Figure 9(a) shows the direct-line-of-sight control image of the GFP-labeled ECs on PDLLA scaffold lumen. The same ROI was then used for fiber scanning followed by fluorescence mapping. Following the process described in Secs. 2.7 and 3.5, we obtained the fluorescence mapped image shown in Fig. 9(b). Comparing the mapped image to the control image, it is clear that the spatial distribution of ECs obtained through fluorescence mapping is in good agreement with the control image. This result confirms that the scanning-fiber-based method can image through a 0.5-mm thick tissue scaffold and reveal the spatial distribution of ECs with single-cell-level resolution. Figure 9(c) shows that the SNR of a single GFP-labeled EC is around two for the 0.5 mm thick PDLLA phantom, which also confirms the reliability of our fluorescence mapping results.

## 4 Discussion

Due to significant photon scattering in turbid biological tissues, a major challenge in biophotonics is the conflict between imaging depth and imaging resolution. Even in the case of photoacoustic imaging, the resolution remains closely linked with imaging depth, where one can realize a spatial resolution of  $>50 \mu\text{m}$  within a depth of three photon TMFP.<sup>11,12</sup> In contrast with other imaging modalities, the method developed here can largely “decouple” the link between imaging depth and imaging resolution. The resolution of our imaging method is essentially determined by the distance between the MIC and the ROI and not by the entire thickness of the scaffold/tissue as demonstrated in Fig. 6. In principle, if system noise is sufficiently small compared with the signal strength generated by the fluorophore, we can maintain single-cell-level imaging resolution at a depth that exceeds the photon TFMP by at least one order of magnitude. In fact, using fluorescent microspheres as sources, we have shown that our imaging method is capable of achieving 20 to 30  $\mu\text{m}$  imaging resolution at an imaging depth exceeding 10 photon TMFPs (0.5 mm thick PDLLA scaffold plus three mm thick porcine skin).

The proper functioning of the imaging method presented here requires that the system signal should be stronger than the noise. This requirement makes intuitive sense: if the fluorescence response of the detector does not change regardless of whether the excitation spot coincides with the fluorophore or not, then it would be very difficult to apply the fluorescence mapping procedure to reconstruct the fluorophore distribution. Given this observation, it is worthwhile to consider several potential sources for system noise. First, we note that the spatial distribution of an excitation spot extends beyond its FWHM. Thus, during noise measurements, even though we moved the excitation spot away from any of the microspheres on the luminal surface, a small portion of the excitation light might overlap with microspheres and contribute towards the noise spectra in Fig. 8. However, noise generated by this effect should not depend significantly on the total thickness of the phantom and therefore cannot explain the reduction in system SNR after adding the porcine skin. Next, we note that during the fiber scanning process, the excitation light was directed towards the luminal surface which generates scaffold autofluorescence along the propagation path. However, the autofluorescence generated by such forward propagating excitation light would only depend on the distance between the MIC and the ROI on the luminal surface, which again is independent of the total phantom thickness. Therefore, to account for the SNR reduction observed between Fig. 8(a) and 8(b), we have to consider the fact that a small portion of the excitation light back-reflects from the luminal surface and propagates towards the exterior surface as illustrated in Fig. 10. After adding the 3-mm thick porcine skin, such back propagating excitation light would induce additional autofluorescence from the porcine skin, which would reduce the overall system SNR. In fact, many effects may induce such back-propagating light. Several examples are the Fresnel reflection at the air/MIC interface, photon scattering at the interface of the MIC and the PDLLA scaffold, and light back-scattering within the turbid PDLLA scaffold, i.e., similar to what occurs in optical coherence tomography. As discussed in Sec. 3.4, the resolution of our imaging system is closely linked to the FWHM of the excitation spot on the luminal surface. The size of the excitation spot is in turn determined by the scaffold optical property as well as the distance between the MIC and the luminal surface, both of which are largely independent of the total phantom thickness. Therefore, as long as the FWHM of the excitation light remains the same and the system SNR is sufficiently large ( $\sim 2$  or higher), the resolution of the fluorescence mapped



**Fig. 9** (a) Control image showing the actual endothelial cell (EC) distribution on scaffold lumen. (b) A fluorescence mapped image of EC distribution that corresponds to the image in (a). Comparison between the control image and the fluorescence mapped image indicates that our method can “see” through a 0.5 mm thick PDLLA scaffold with single-cell-level resolution. (c) signal-to-noise measurement for a single green fluorescent protein (GFP)-labeled EC on scaffold lumen. The SNR is around two for a 0.5 mm thick PDLLA phantom.

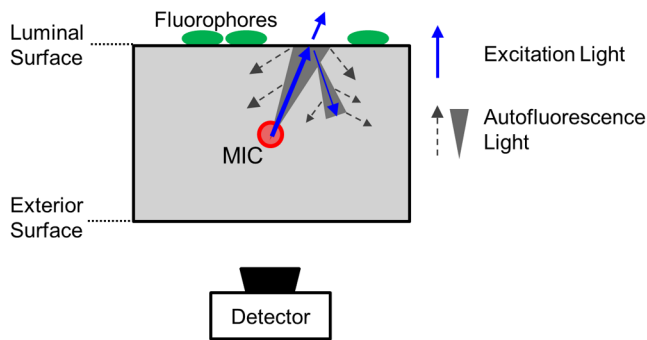


**Fig. 10** A schematic showing the potential sources for imaging system noise.

images should not depend critically on the overall thickness of the optical phantom, as can be seen from Fig. 6.

We note that the scanning-fiber-based method is well suited for tissue engineering applications. For example, the process of scaffold fabrication—a necessary step in tissue engineering—can be easily modified for embedding MICs. With proper design, we can essentially place an MIC anywhere within the tissue scaffold. Therefore, once an ROI is selected (e.g., lumen in the case of vessel engineering), we can place the MIC in close proximity to the ROI to achieve single-cell-level resolution. Secondly, since fluorescence mapping only requires total fluorescence intensity, we do not require a high numerical aperture objective lens. As a result, our imaging system can provide more than 10 cm in working distance, which is more than sufficient for the geometrical constraints imposed by most bioreactors currently in use. We point out that this practical constraint is actually very stringent in tissue engineering practices. For example, most of the commercial two-photon microscopes require focusing excitation light within a sub- $\mu\text{m}$  spot, which can only be achieved by using high numerical aperture objectives.<sup>23</sup> Such a high numerical aperture, however, generally leads to a much shorter working distance, which makes it cumbersome to integrate a functional bioreactor with a commercial two-photon or confocal microscope. A few recent examples of these types of work can be found.<sup>25,26</sup> We point out that the systems described in both references are very complex. Such complexity is mainly due to the conflict between the large geometrical dimension of a functional bioreactor and the extremely short working distance of a confocal or a two-photon microscope.

In the future, we plan to utilize the imaging method developed here for other tissue engineering studies. We are currently combining the imaging instruments with a pulsatile fluid flow bioreactor for blood vessel bioengineering studies. For such *in vitro* applications, the capability of performing non-destructive and single-cell-level imaging has a significant advantage: since we no longer need to remove the vessel from the bioreactor and subject it to frequent dissection and histological analyses, we can dynamically monitor how ECs proliferate, migrate, and respond to external stimuli such as fluid shear stress and pulsation. Given the high optical scattering within the scaffold and the geometrical constraints of the bioreactor, such a study has yet to be carried out in tissue engineering.<sup>14</sup> As a result, some of the most critical questions in tissue engineering, such as cell-cell interaction, cell-scaffold interaction, and the mechanism of neovascularization, remain not well understood. The main limitation of our method is the underlying assumption that

fluorescent-labeled cells are distributed over a 2-D surface. However, for studies involving ECs, this assumption is indeed valid and should not pose any problems. With appropriate modifications, we can potentially apply the method developed here to monitor the preconditioning of other hollow cavity tissues such as bladder, trachea, or colon, where epithelial cells play an important role in the biologically complex process of tissue regeneration.

The experimental results in this paper (Figs. 6–9) suggests that as long as the fluorescent signal is significantly stronger than scaffold autofluorescence, the resolution of our imaging system does not depend critically on system SNR and does not degrade significantly as the imaging depth increases. For example, fluorescence mapped images in Fig. 6 have almost identical image resolution despite the fact that their SNRs are quite different. Our result and analysis indicate that in order to achieve maximal imaging depth, which is very important for future *in vivo* studies, we should select a fluorophore whose emission spectrum has minimal overlap with scaffold or tissue autofluorescence. Given the spectral data in Fig. 9(b), it is clear that using a biomarker such as near-infrared quantum dots (QDs) with emission peak above 650 nm would be ideal. Such QDs can be excited by the blue laser (473 nm) used in this work. Due to the very weak autofluorescence noise at the excitation wavelength of 473 nm, we should be able to further improve imaging depth to be greater than three mm while maintaining 20 to 30  $\mu\text{m}$  image resolution. The fluorophores we used in this study unfortunately have significant spectral overlap with scaffold autofluorescence. Consequently, it is very difficult to precisely determine how much of the system noise is generated by the fluorophores and how much is caused by scaffold autofluorescence. Using the QD-labeled ECs may also enable us to more accurately quantify the behaviors of system SNRs under different tissue/scaffold thicknesses.

## 5 Conclusion

We have developed a scanning-fiber-based imaging method that can perform deep-tissue imaging with single-cell-level resolution. Our method is based on directly embedding one or more hollow core fibers within a tissue scaffold as MICs. By inserting fiber micro-mirrors into the MICs, we can locally deliver excitation light towards a specific ROI and excite the fluorophores contained within. After collecting fluorescent signals and mapping them onto a digital grid based on fiber micro-mirror location, we can reconstruct the spatial distribution of the fluorophores within the ROI. Using an optical phantom composed of fluorescent microspheres, a 500- $\mu\text{m}$  thick tissue scaffold, and a 3-mm thick porcine skin, we have demonstrated the decoupling between imaging depth and imaging resolution. Specifically, we have shown that the resolution of our fluorescence mapping results does not degrade even after we introduce the additional 3-mm thick porcine skin to the total imaging depth. As a result, we have achieved 20 to 30  $\mu\text{m}$  resolution at an imaging depth of more than 10 photon TMFPs. Finally, we have shown that we can spatially resolve single GFP-labeled ECs through a 500  $\mu\text{m}$  thick scaffold with a photon TMFP of 170  $\mu\text{m}$ .

## Acknowledgments

We would like to thank Dr. Joseph Freeman in the Department of Biomedical Engineering at Rutgers University for his advice on scaffold sintering. This research was funded by a grant from

the National Institutes of Health (NIBIB, HL098912), the National Science Foundation (CBET 0955072), and the Institute for Critical Technology and Applied Science (Holey Scaffolds, Virginia Tech).

## References

1. A. Atala et al., "Tissue-engineered autologous bladders for patients needing cystoplasty," *The Lancet* **367**(9518), 1241–1246 (2006).
2. C. T. Laurencin and J. W. Freeman, "Ligament tissue engineering: an evolutionary materials science approach," *Biomaterials* **26**(36), 7530–7536 (2005).
3. A. Raya-Rivera et al., "Tissue-engineered autologous urethras for patients who need reconstruction: an observational study," *The Lancet* **377**(9772), 1175–1182 (2011).
4. S. Petit-Zeman, "Regenerative medicine," *Nat. Biotechnol.* **19**(3), 201–206 (2001).
5. R. M. Nerem and A. Sambanis, "Tissue engineering: from biology to biological substitutes," *Tissue Eng.* **1**(1), 3–13 (1995).
6. N. D. Evans and M. M. Stevens, "Complexity in biomaterials for tissue engineering," *Nat. Mater.* **8**(6), 457–470 (2009).
7. M. P. Lutolf and J. A. Hubbell, "Synthetic biomaterials as instructive extracellular microenvironments for morphogenesis in tissue engineering," *Nat. Biotechnol.* **23**(1), 47–55 (2005).
8. L. G. Griffith and G. Naughton, "Tissue engineering—current challenges and expanding opportunities," *Science* **295**(5557), 1009–1014 (2002).
9. V. Ntziachristos, "Going deeper than microscopy: the optical imaging frontier in biology," *Nat. Meth.* **7**(8), 603–614 (2010).
10. D. J. Stephens and V. J. Allan, "Light microscopy techniques for live cell imaging," *Science* **300**(5616), 82–86 (2003).
11. H. F. Zhang et al., "Functional photoacoustic microscopy for high-resolution and noninvasive in vivo imaging," *Nat. Biotechnol.* **24**(7), 848–851 (2006).
12. V. Ntziachristos et al., "Fluorescence molecular tomography resolves protease activity in vivo," *Nat. Med.* **8**(7), 757–761 (2002).
13. J. Stitzel et al., "Controlled fabrication of a biological vascular substitute," *Biomaterials* **27**(7), 1088–1094 (2006).
14. S. J. Lee et al., "In vitro evaluation of electrospun nanofiber scaffolds for vascular graft application," *J. Biomed. Mater. Res. Part A* **83**(4), 999–1008 (2007).
15. S. Kaushal et al., "Functional small diameter neovessels using endothelial progenitor cells expanded ex vivo," *Nat. Med.* **7**(9), 1035–1040 (2001).
16. S. J. Lee et al., "Development of a composite vascular scaffolding system that withstands physiological vascular conditions," *Biomaterials* **29**(19), 2891–2898 (2008).
17. B. W. Tillman et al., "The in vivo stability of electrospun polycaprolactone-collagen scaffolds in vascular reconstruction," *Biomaterials* **30**(4), 583–588 (2009).
18. T. Shinoka et al., "Creation of viable pulmonary artery autografts through tissue engineering," *J. Thorac. Cardiovasc. Surg.* **115**(3), 536–546 (1998).
19. Q. P. Pham, U. Sharma, and A. G. Mikos, "Electrospinning of polymeric nanofibers for tissue engineering applications: a review," *Tissue Eng.* **12**(5), 1197–1211 (2006).
20. L. D. Wright et al., "Fabrication and mechanical characterization of 3D electrospun scaffolds for tissue engineering," *Biomed. Mater.* **5**(5), 055006 (2010).
21. S. A. Prael, M. J. C. van Gemert, and A. J. Welch, "Determining the optical properties of turbid media by using the adding, Å doubling method," *Appl. Opt.* **32**(4), 559–568 (1993).
22. W. F. Cheong, S. A. Prael, and A. J. Welch, "A review of the optical properties of biological tissues," *IEEE J. Quantum Elect.* **26**(12), 2166–2185 (1990).
23. F. Helmchen and W. Denk, "Deep tissue two-photon microscopy," *Nat. Meth.* **2**(12), 932–940 (2005).
24. T. D. Wang et al., "Confocal fluorescence microscope with dual-axis architecture and biaxial postobjective scanning," *J. Biomed. Opt.* **9**, 735–742 (2004).
25. J. A. Kluge et al., "Bioreactor system using noninvasive imaging and mechanical stretch for biomaterial screening," *Ann. Biomed. Eng.* **39**(5), 1390–1402 (2011).
26. L. E. Niklason et al., "Enabling tools for engineering collagenous tissues integrating bioreactors, intravital imaging, and biomechanical modeling," *Proc. Natl. Acad. Sci.* **107**(8), 3335–3339 (2010).